Accepted for publication in **Computational Materials Science**, July 2015

# Numerical simulations of crack propagation in screws with phase-field modeling

D. Wick * T. Wick † R. J. Hellmig ‡ H.-J. Christ §

In this work, we consider a phase-field framework for crack propagation problems in elasticity and elasto-plasticity. We propose a rate-dependent formulation for solving the elasto-plastic problem. An irreversibility constraint for crack evolution avoids non-physical healing of the crack. The resulting coupled two-field problem is solved in a decoupled fashion within an augmented Lagrangian approach, where the latter technique treats the crack irreversibility constraint. The setting is quasi-static and an incremental formulation is considered for temporal discretization. Spatial discretized is based on a Galerkin finite element method. Both subproblems of the two-field problem are nonlinear and are solved with a robust Newton method in which the Jacobian is built in terms of analytically derived derivatives. Our algorithmic developments are demonstrated with several numerical tests that are motivated by experiments that study failure of screws under loading. Therefore, these tests are useful in practice and of high relevance in mechanical engineering. The geometry and material parameters correspond to realistic measurements. Our goal is a comparison of the final crack pattern in simulation and experiment.

## 1 Introduction

Presently, crack propagation in solids is one of the major research topics in energy, environmental, and mechanical engineering. Consequently, many models and numerical techniques have been investigated to date. Specifically, Griffith's model [1] for quasi-static fracture evolution has been successfully applied. Here, the crack propagates if the rate of elastic energy dissipation per unit surface area of the increment step is equal to a critical energy release rate $G_c$; if it is less, the crack does not move. On the contrary, it is unstable if $G_c$ exceeds the critical value. Griffith found that $G_c$ is related to the crack surface energy increase. In the case of isotropic linear materials, the critical energy release rate is linked to the stress intensity factor.

*Institut für Werkstofftechnik, Universität Siegen, D-57068 Siegen, Germany; and EJOT GmbH & Co. KG, D-57319 Bad Berleburg, Germany; dominik.wick@uni-siegen.de

†Johann Radon Institute for Computational and Applied Mathematics (RICAM), Austrian Academy of Sciences, Altenberger Str. 69, 4040 Linz, Austria; and Fakultät für Mathematik, Lehrstuhl M17, Technische Universität München, 85747 Garching bei München, Germany; thomas.wick@ricam.oeaw.ac.at; Corresponding author

‡EJOT GmbH & Co. KG, D-57319 Bad Berleburg, Germany; and Institut für Werkstofftechnik, Universität Siegen, D-57068 Siegen, Germany; rhellmig@ejot.de

§Institut für Werkstofftechnik, Universität Siegen, D-57068 Siegen, Germany; christ@ifwt.mb.uni-siegen.de

The solution of crack representation and propagation requires special techniques for their numerical treatment. In recent years, different approaches have been proposed such as the extended finite element method (XFEM) by [2] and generalized finite elements (GFEM) methods [3] both based on the partition of unity method of [4] in which the displacement field is enriched with discontinuities. In the last decade, variational and phase-field techniques for crack propagation in solid mechanics have gained increased interest. The original model has been proposed by Francfort and Marigo [5]. Numerical simulations and mathematical investigation has been subject, e.g., in [6, 7]. An important extension towards a thermodynamically-consistent phase-field formulation has been suggested by Miehe et al. [8, 9] and further simulations and numerical extensions (also by other researchers) are found in [10, 11, 12]. Specifically, a finite element framework for multiphysics phase-field simulations has been presented in [13]. Instead of modeling the discontinuities explicitly (like in XFEM and GFEM), employing phase-field, the lower-dimensional crack surface is approximated with an auxiliary function $\varphi$ with values 0 in the crack and 1 in the undamaged material; an illustration by means of a numerical simulation is provided in Figure 2. Furthermore, $\varphi$ smoothly interpolates between 0 and 1 leading to a diffusive transition zone that is of size $\varepsilon$, a so-called length-scale model regularization parameter. From a computational point of view, the phase-field approach is attractive since crack nucleation, length increment, and the path are automatically included in the model [7]. On the other hand, the diffusive transition zone tends to smear out the sharp crack surface and the characteristic length-scale parameter $\varepsilon$ must be chosen accordingly. Here, an adaptive local grid refinement technique can be used to increase crack surface resolution while keeping the computational cost low. Additionally, some of the challenges associated with a non-convex energy functional require careful developments as outlined and addressed in [7, 14, 15].

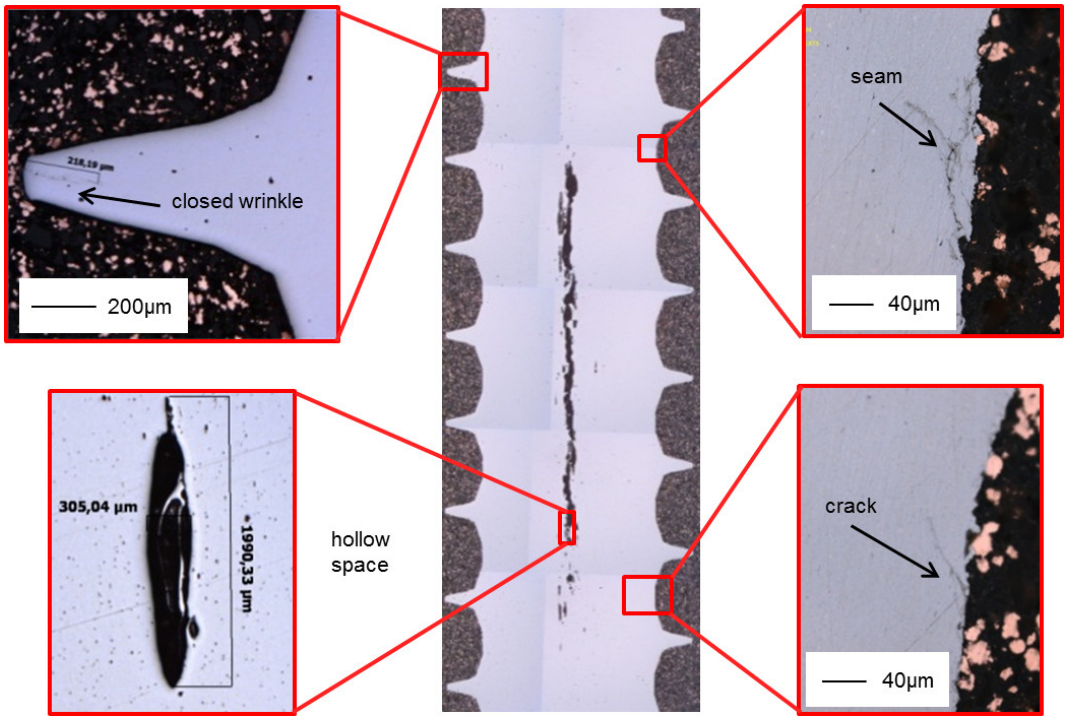


Figure 1: Illustration and characteristic length scales for material damage in screws.

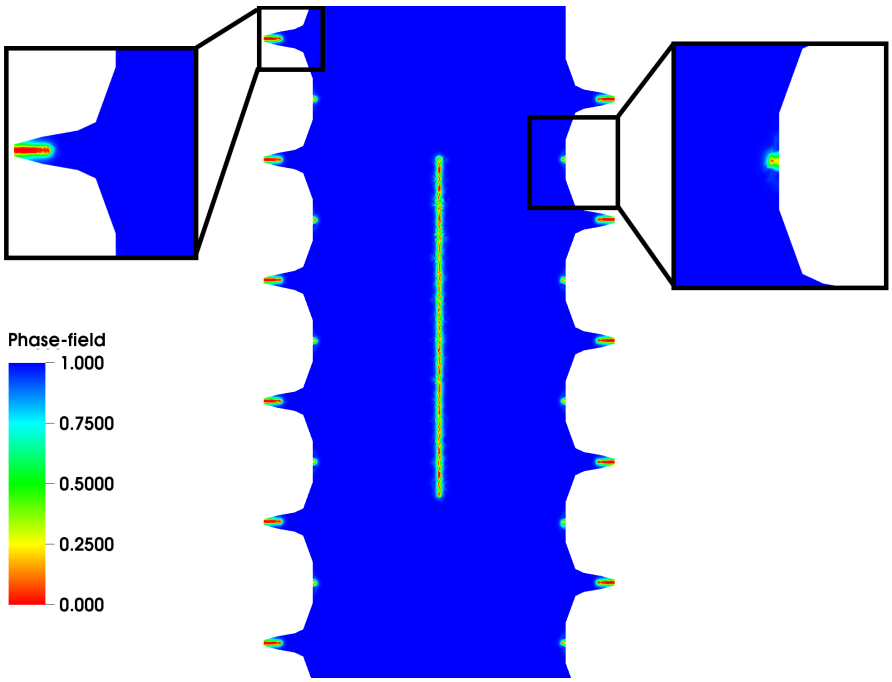


Figure 2: Initialization of cracks modeled with phase-field. Crack pattern are described with an indicator function $\varphi$ (i.e., the phase-field function) with 0 values in the crack (red color) and 1 (blue color) in the undamaged zone. The diffusive transition zone has width $\varepsilon$ (green/yellow) and here the phase-field function has values that smoothly vary between 0 and 1. This color scale is also employed in Section 4 to visualize cracks and damage in terms of the phase-field variable.

While it is fairly well understood how phase-field fracture models act in brittle materials with elasticity, only a few references exist to date on ductile crack propagation (e.g., [16, 17, 18, 19]). Here, the last reference focuses on numerical tests of I-shaped specimen that have some similarities to screw simulations as we have them in mind. From phase-field modeling point of view our proposed approach for fracture propagation in elasto-plastic materials has similarities with the technique described in [18] in which quasi-static brittle fracture propagation in elasto-plastic solids has been formulated.

Our first aim in this paper is an algorithmic extension of elasto-plastic phase-field fracture combined with an augmented Lagrangian formulation for treating the crack irreversibility [12]. This approach is modeled in terms of a rate-dependent formulation [20] in which continuous time derivatives are approximated with a backward in time difference quotient, i.e.,

$$\partial_t \varphi \approx \varphi - \varphi^{m-1} \leq 0.$$

Here, $\varphi$ denotes the phase-field fracture variable and $\varphi^{m-1}$ its state at the previous time step $t^{m-1}$. Spatial discretization is done with finite elements, which are well-known in solid mechanics. Due to the crack irreversibility and the elasto-plastic material behavior the resulting scheme has two types of nonlinearities for which a robust Newton solver is employed. The capabilities of our approach are substantiated with a benchmark example. Several screw tests constitute the main goal that include comparisons with crack growth in elasticity and elasto-plasticity as well as comparative studies of crack pattern in experiments and finite element simulations. The latter aspect has presently high relevance in mechanical engineering.

In summary, the importance of our present paper is twofold:

- Formulating elasto-plastic crack propagation with a thermodynamically consistent phase-field model and its rate-dependent formulation within a robust augmented Lagrangian solution algorithm.
- Investigation of material damages that are presently of high importance in mechanical engineering for learning reasons for material damage and failure. Figure 1 shows some characteristics of material damage in screws. Typical material damages are closed wrinkles in the middle of thread flanks, seams, cracks and hollow-rolled screws. The cause of material damage is often a wrong set up of the rolling machine. We note that in the production process, the thread of the final screw is obtained from rolling of an initially un-machined blank. Consequently, numerical simulations (here with phase-field; see Figure 2) greatly help to better understand the mechanisms of failure.

The outline of this paper is as follows: In Section 2, the model and corresponding variational formulation are presented. Next in Section 3, the finite element discretization is discussed. Finally in Section 4, several numerical tests are computed that include benchmarks and comparison with experimental findings.

## 2 The energy functional and corresponding weak formulation

### 2.1 Preliminaries to plasticity modeling

Our plasticity model is based on the theory of linear-elastic perfectly plastic material [20]. This model has been extensively investigated and benchmarked in [21] (we refer specifically to [22] for an adaptive finite element implementation from which we take some algorithmic ideas) and also implemented in the underlying programming code [23, 24]. This model needs to be formulated for tensor-valued quantities, i.e., we are seeking for vector-valued displacements $u$ such that:

$$\sigma(u) = Ce(u)$$

where $\sigma := \sigma_{ij}$ is the stress tensor, $e := e_{kl}$ the strain tensor, and $C := C_{ijkl}$ is a fourth-order stiffness material tensor. Specifically, we formulate the problem in a domain $\Omega$ with the boundaries $\partial\Omega := \Gamma_D \cup \Gamma_N$ where we impose displacement Dirichlet conditions on $\Gamma_D$ and traction Neumann conditions on $\Gamma_N$ in variational form (that is related to the principle of virtual work) as follows:

$$\int_\Omega \Pi(\sigma(u)) : e(w)\, dx = \int_{\Gamma_N} g \cdot w\, ds \quad \text{for all test functions } w, \tag{1}$$

where $\Pi$ is a projection operator that is defined below and $g$ stands for some traction force. We use the symmetric strain tensor $e(u) := \frac{1}{2}(\nabla u + \nabla u^T)$, and the symmetric stress tensor $\sigma$ is defined as

$$\sigma(u) := Ce(u) := 2\mu_s e(u)^D + \lambda_s \cdot tr(e(u))I,$$

where $tr(\cdot)$ denotes the trace, $I$ the identity matrix, and $\mu$ and $\lambda$ are the Lamé coefficients, and their relationship to the elastic modulus and Poisson's ratio is given by:

$$\nu_s = \frac{\lambda_s}{2(\lambda_s + \mu_s)}, \qquad E = \frac{\mu_s(\lambda_s + 2\mu_s)}{(\lambda_s + \mu_s)},$$
$$\mu_s = \frac{E}{2(1+\nu_s)}, \qquad \lambda_s = \frac{\nu_s E_s}{(1+\nu_s)(1-2\nu_s)}.$$

Furthermore, $\tau^D$ is the deviatoric part of a tensor $\tau$, in two dimensions defined as

$$\tau^D := \tau - \frac{1}{2} tr(\tau) I.$$

The main difference with respect to a pure elastic setting is the projection operator $\Pi$, which is defined as:

$$\Pi(\tau) = \begin{cases} \tau & |\tau^D| \leq \sigma_0, \\ \sigma_0 |\tau^D|^{-1} \tau^D + \frac{1}{2} tr(\tau) I & |\tau^D| > \sigma_0. \end{cases}$$

## 2.2 The energy functional

For a given crack $\mathcal{C}$ in a domain $\Omega$, the total energy reads:

$$E(\eta, \mathcal{C}) = \frac{1}{2} \int_{\Omega \setminus \mathcal{C}} \Pi(\sigma) : e(u)\, dx - \int_{\partial_N \Omega} \tau \cdot \eta\, ds + G_c \mathcal{H}^{d-1}(\mathcal{C}). \tag{2}$$

The regularized functional in which the crack energy is approximated using an additional solution variable $\varphi$ (the phase-field) and an elliptic functional [25, 26] reads:

$$\begin{aligned} E_\varepsilon(\eta, \varphi) = \frac{1}{2} \int_\Omega \big((1-\kappa)\varphi^2 + \kappa\big) \Pi(\sigma) : e(u)\, dx - \int_{\partial_N \Omega} \tau \cdot u\, ds \\ + G_c \int_\Omega [\frac{1}{2\varepsilon}(1-\varphi)^2 + \frac{\varepsilon}{2} (\nabla \varphi)^2]\, dx, \end{aligned} \tag{3}$$

where $\kappa$ is a positive regularization parameter for elastic energy, with $\kappa \ll \varepsilon$. In the following, we explain the meaning of the different terms in (3). The first term denotes the elastic bulk energy, the middle term traction forces at Neumann boundaries $\partial_N \Omega$, and the final term characterizes the surface energy of the crack.

The model is completed by a thermodynamically consistent formulation[1] as proposed in [8] in which we only allow for crack growth (irreversibility) but no healing:

$$\partial_t \varphi \leq 0.$$

This leads to the final energy functional

$$\begin{aligned} E_\varepsilon(\eta, \varphi) = \frac{1}{2} \int_\Omega \big((1-\kappa)\varphi^2 + \kappa\big) \Pi(\sigma) : e(u)\, dx - \int_{\partial_N \Omega} \tau \cdot u\, ds \\ + G_c \int_\Omega [\frac{1}{2\varepsilon}(1-\varphi)^2 + \frac{\varepsilon}{2} (\nabla \varphi)^2]\, dx + I_K(\varphi^{m-1})(\varphi^n), \end{aligned} \tag{4}$$

where $I_K(\cdot)(\cdot)$ denotes an indicator function representing the irreversibility condition. Here, $\varphi^{m-1}$ denotes the phase-field value at the previous time step $t^{m-1}$. In the next section, we use an augmented Lagrangian formulation to specify $I_K(\cdot)(\cdot)$.

## 2.3 The Euler-Lagrange equations in a rate-dependent weak formulation

Our aim in this section is to describe our solution algorithm in detail. In order to apply a Galerkin finite element method, we need to derive the Euler-Lagrange equations from the energy functional (3).

[1] In this paper, we do not deal with cracks under compression that adds a stress decomposition to the full model proposed in [8]. For discussion and further studies, we refer to [8, 9, 10, 15].

### 2.3.1 A Hencky-type formulation for phase-field elasto-plasticity

First, we formulate a Hencky-type problem [20] in which the solid equation is treated as to be fully stationary while time-dependence appears in the irreversibility constraint of the phase-field equation. The resulting problem is quasi-stationary because of the constraint $\partial_t \varphi \leq 0$ and 'time' is characterized in terms of a loading parameter. Our two-field problem can then be formulated as follows. Let $V$ and $W$ denote Hilbert function spaces. Find the vector-valued displacement $u$ such that:

$$\int_\Omega \left((1-\kappa)\varphi^2 + \kappa\right) \Pi\sigma(u) : e(w)\, dx - \int_{\Gamma_N} g \cdot w\, ds = 0 \quad \forall w \in V, \tag{5}$$

as well as the scalar-valued phase-field variable $\varphi$:

$$\begin{aligned}
&(1-\kappa) \int_\Omega [\varphi\, \Pi(\sigma(u)) : e(u)]\, \psi\, dx \\
&\quad + G_c \int_\Omega \Big( -\frac{1}{\varepsilon}(1-\varphi)\, \psi + \varepsilon \nabla\varphi \cdot \nabla\psi \Big)\, dx \\
&\quad + \int_\Omega \Big( (\lambda + \gamma(\varphi - \varphi^{m-1}))^+ \psi \Big)\, dx = 0 \quad \forall\, \psi \in W.
\end{aligned} \tag{6}$$

The index set $I_K(\cdot)(\cdot)$ (defined in functional (4)) is specified in equation (6) via its augmented Lagrangian formulation

$$\int_\Omega \Big( (\lambda + \gamma(\varphi - \varphi^{m-1}))^+ \psi \Big),$$

where $\gamma$ denotes the penalization parameter and $\lambda$ an update function. Furthermore, $(f)^+$ denotes the positive part a function, i.e., $(f)^+ := max\{f(x), 0\}$. Details of its derivation and algorithmic details of such a formulation are outlined in [12].

In order to solve both problems, we formulate a semi-linear form for the nonlinear elasto-plasticity part and a semi-linear form for the nonlinear phase-field as follows:

**Formulation 2.1** (Phase-field for Hencky-type elasto-plasticity)**.** Find a vector-valued displacement $u \in V$ such that:

$$A_1(u)(w) = \int_\Omega \left((1-\kappa)\varphi^2 + \kappa\right) \Pi\sigma(u) : e(w)\, dx - \int_{\Gamma_N} g \cdot w\, ds = 0 \quad \forall w \in V, \tag{7}$$

and find a scalar-valued phase-field $\varphi$ such that:

$$\begin{aligned}
A_2(\varphi)(\psi) = &(1-\kappa) \int_\Omega [\varphi\, \Pi e(u) : e(u)]\, \psi\, dx \\
&+ G_c \int_\Omega \Big( -\frac{1}{\varepsilon}(1-\varphi)\, \psi + \varepsilon \nabla\varphi \cdot \nabla\psi \Big)\, dx \\
&+ \int_\Omega \Big( (\lambda + \gamma(\varphi - \varphi^{m-1}))^+ \psi \Big)\, dx \\
&= 0 \quad \forall\, \psi \in W.
\end{aligned} \tag{8}$$

### 2.3.2 A Prandl-Reuss formulation for phase-field elasto-plasticity

In extension to the Hencky-type model, a rate-dependent process formulated in terms of a quasi-stationary Prandl-Reuss setting is proposed in this work. Following [20, 22], we consider

$$Ce(\partial_t u) = \partial_t \sigma(u).$$

Then, the variational form reads in each loading step $m$:

$$\int_\Omega \sigma^m(u) : e(w)\,dx = \int_{\Gamma_N} g^m \cdot w\,ds \quad \forall w \in V, \quad m = 1, 2, 3, \ldots. \tag{9}$$

Now, we discretize $Ce(\partial_t u) = \partial_t \sigma(u)$ in time with a backward difference quotient and we obtain

$$\begin{aligned} & Ce(\partial_t u) = \partial_t \sigma(u) \\ \Rightarrow \quad & Ce(\frac{u^m - u^{m-1}}{\Delta t}) = \frac{\sigma^m(u) - \sigma^{m-1}(u)}{\Delta t} \\ \Rightarrow \quad & Ce(u^m - u^{m-1}) + \sigma^{m-1}(u) = \sigma^m(u) \end{aligned}$$

where $\Delta t := t^m - t^{m-1}$ denotes the time step size. Furthermore, $u^m$ and $\sigma^m$ denote the current displacement and stress values, respectively. Similarly, $u^{m-1}$ and $\sigma^{m-1}$ denote the previous time step (i.e., loading step) displacement and stress values, respectively. Since we deal with the previously introduced plasticity law, we insert the projection operator $\Pi$ such that

$$\sigma^m(u) = \Pi(\sigma^{m-1}(u) + Ce(u^m - u^{m-1}))$$

at each time $t^m$. We note that the stress-strain relation is now nonlinear. In a linear setting (e.g., linear elasticity), there would be no difference between this formulation and the stationary forms. Then, we insert this term into Equation (9):

$$\begin{aligned} \int_\Omega \sigma^m(u) : \varepsilon(w)\,dx &= \int_\Omega \Pi(\sigma^{m-1} + Ce(u^m - u^{m-1})) : \varepsilon(w)\,dx \\ &= \int_{\Gamma_N} g^m \cdot w\,ds, \quad m = 1, 2, 3, \ldots. \end{aligned} \tag{10}$$

Next, we formulate the two-field problem:

**Formulation 2.2** (Phase-field for Prandl-Reuss elasto-plasticity)**.** Find vector-valued displacements $u \in V$ for each loading step $m = 1, 2, 3, \ldots$ such that:

$$\begin{aligned} A_1(u)(w) &= \int_\Omega \left((1-\kappa)\varphi^2 + \kappa\right) \Pi(\sigma^{m-1} + Ce(u^m - u^{m-1})) : e(w)\,dx - \int_{\Gamma_N} g \cdot w\,ds \\ &= 0 \quad \forall w \in V, \end{aligned} \tag{11}$$

and find a scalar-valued phase-field $\varphi$ for $m = 1, 2, 3, \ldots$ such that:

$$\begin{aligned} A_2(\varphi)(\psi) = {} & (1-\kappa) \int_\Omega \varphi\, \Pi(\sigma^{m-1} + Ce(u^m - u^{m-1})) : e(u) \cdot \psi\,dx \\ & + G_c \int_\Omega \Big(-\frac{1}{\varepsilon}(1-\varphi)\,\psi + \varepsilon(\nabla\varphi \cdot \nabla\psi\Big)\,dx \\ & + \int_\Omega (\lambda + \gamma(\varphi - \varphi^{m-1}))^+\,\psi\,dx \\ = {} & 0 \quad \forall\, \psi \in W. \end{aligned} \tag{12}$$

## 3 Finite element discretization and solution algorithm

The continuous problems are discretized in space with a Galerkin finite element scheme. The computational domain is subdivided into quadrilateral elements. Both subproblems are discretized using $H^1$-conforming bilinear elements, i.e., the trial and test space uses $Q_1^c$-finite elements. Consequently, the discrete spaces have the property $V_h \subset V$ and $W_h \subset W$. The proposed augmented Lagrangian solution algorithm is based on a decoupling of the solid and phase-field equations, allowing for sophisticated solvers for both subproblems.

Specifically, we solve as follows:

- Given $\varphi$ from a previous step, find the current $u$;
- Given the just computed $u$, find the new $\varphi$.

Furthermore, the two subproblems are nonlinear and are treated with a robust Newton solver that includes a simple backtracking line search algorithm.

We begin with the decoupled solution of the inner problems. For any given phase-field $\varphi^h \in W_h$ we find $u^h \in V_h$ by solving the nonlinear problem using a defect-correction scheme of Newton's method for the iteration steps $m = 0, 1, 2, \ldots$

$$\begin{aligned} A_1'(u^{h,m})(\delta u^h, w) &= -A_1(u^{h,m})(w) \quad \forall w \in V_h, \\ u^{h,m+1} &= u^{h,m} + \omega \delta u^h, \end{aligned} \tag{13}$$

with a line search parameter $\omega \in (0, 1]$. Here, we need the Jacobian of $A_1(u)(w)$ applied to a direction $\delta u$ that is derived by using analytical expressions in order to maintain superlinear (or quadratic) convergence.

$$\begin{aligned} A_1'(u)(\delta u, w) &= \int_\Omega \left((1-\kappa)\varphi^2 + \kappa\right) \Pi'(\sigma^{m-1} + Ce(u^m - u^{m-1}))(\delta u) : e(w)\, dx \\ &= 0 \quad \forall w \in V, \end{aligned} \tag{14}$$

where the derivative of $\Pi$ is given by

$$\Pi'(\tau)(\delta\tau) = \begin{cases} \delta\tau & |\tau^D| \le \sigma_0, \\ \sigma_0 |\tau^D|^{-1} \delta\tau^D - \sigma_0 |\tau^D|^{-d} \tau \delta\tau^D + \frac{1}{2} tr(\delta\tau) I & |\tau^D| > \sigma_0, \end{cases}$$

where $d = 2$ (the problem dimension).

Similarly as for the Newton scheme (13), such a nonlinear iteration is defined for solving phase-field problem. Here, we compute as derivative into a direction $\delta\varphi$:

$$\begin{aligned} A_2'(\varphi)(\delta\varphi, \psi) = (1-\kappa) &\int_\Omega \delta\varphi\, \Pi(\sigma^{m-1} + Ce(u^m - u^{m-1})) : e(u) \cdot \psi\, dx \\ &+ G_c \int_\Omega \Big( -\frac{1}{\varepsilon} \delta\varphi \cdot \psi + \varepsilon \nabla\delta\varphi : \nabla\psi \Big)\, dx \\ &+ \gamma \int_{\mathcal{A}(\phi)} \delta\varphi : \psi\, dx \end{aligned} \tag{15}$$

where

$$\mathcal{A}(\phi) = \{x \in (0, L)^3 \,|\, \lambda + \gamma(\phi - \phi^{m-1}) > 0\}.$$

A crucial role for nonlinear problems includes the appropriate determination of $\omega$. A simple strategy is to modify the update step in (13) as follows: For given $\omega \in (0,1)$ determine the minimal $l^* \in \mathbb{N}$ via $l = 0, 1, \ldots, N_l$, such that

$$R(u_{h,l}^{m,j+1}) < R(u_{h,l}^{m,j}),$$
$$u_{h,l}^{m,j+1} = u_h^{m,j} + \lambda^l \delta u_h^m.$$

For the minimal $l$, we set

$$u_h^{m,j+1} := u_{h,l^*}^{m,j+1}.$$

In this context, the nonlinear residual $R(\cdot)$ is defined as

$$R(u_h^m) := \max_i \left\{ A_1(u_h^m)(w_i) \right\} \quad \forall u_h^m \in V_h,$$

where $\{w_i\}$ denotes the nodal basis of $V_h$. Finally, the linear equation systems within the Newton method are solved with an appropriate linear solver. This Newton strategy has been implemented in [27] and successfully employed for other multiphysics problems. The solution process is outlined in Algorithm 1.

**Algorithm 1** Solution algorithm

At each loading step $t^m$
**repeat**
  Solve augmented Lagrangian loop
  **repeat**
    Solve two-field problem iteratively, namely
      Solve nonlinear elasto-plasticity in Problem 11 with
      Newton's method
      Solve nonlinear phase-field in Problem 12 with
      Newton's method.
  **until** Stopping criterion

$$\max(\|u_{k-1} - u_k\|, \|\varphi_{k-1} - \varphi_k\|) \leq \text{TOL}, \quad \text{TOL} > 0$$

  for the two-field iteration is satisfied
  Update

$$\lambda_{k+1} = (\lambda_k + \gamma(\varphi_{k+1} - \varphi^{m-1}))^+$$

**until** Stopping criterion

$$\|\lambda_{k-1} - \lambda_k\| \leq \text{TOL}, \quad \text{TOL} > 0$$

for augmented Lagrangian is satisfied
Set: $(u^m, \varphi^m) := (u_k, \varphi_k)$.
Increment $t^m \to t^{n+1}$.

Finally, we notice that we employ in the numerical examples local mesh adaptivity with hanging nodes to reduce the computational cost. This can be further extended to dynamic refinement where the mesh could be refined according to either the maximum stress or the phase-field variable as indicator. The latter approach has been successfully applied in [15] with an extension to predictor-corrector mesh adaptivity in which the number of mesh cells grows together with the crack leading to very cost-efficient scheme.

# 4 Numerical results

We perform several numerical tests. First we begin with a benchmark in Section 4.1. Our main focus is afterwards on a two-dimensional cut of a screw with realistic geometry and material parameters. In addition, the finite element simulation results of the final crack pattern are compared to experimental findings of screw failure. All tests are undertaken with the finite element software package deal.II [24].

## 4.1 CT-tests

In this first example, we compute the single edge notched tension test. We use this test for code verification for standard examples in pure elasticity and elasto-plasticity. The geometric and material properties are the same as used in [9]. The configuration is displayed in Figure 3.

The elasticity of solids is characterized by the Poisson ratio $\nu_s$ ($\nu_s < \frac{1}{2}$ for compressible materials) and the Young modulus $E$. From steel, measured at 20° Celsius room temperature, we know that Young's modulus $E = 210GPa$ and Poisson's ratio $\nu_s = 0.3$. Consequently, we obtain $\mu = 80.77kN/mm^2$, $\lambda = 121.15kN/mm^2$ and $G_c = 2.7N/mm$. For the elasto-plasticity test, the plastic flow rule is chosen as $\sigma_0 = \sqrt{2/3} \cdot 450$ [21] and fixed.

The crack growth is driven by a non-homogeneous Dirichlet condition for the displacement field on $\Gamma_{top}$, the top boundary of $\Omega$. We increase the displacement on $\Gamma_{top}$ at each time step, namely

$$u_y = \Delta t \times \bar{u}, \quad \bar{u} = 1 \text{ mm}.$$

Furthermore, we set $\kappa = 10^{-10}h, \epsilon = 2h$ mm and the minimal mesh size parameter is $h \sim 2.2\times10^{-2}mm$. Computations are shown for the time step size $\Delta t = 10^{-4}s$.

We evaluate the surface load vector on the $\Gamma_{top}$ as

$$\tau = (F_x, F_y),$$

where we are particularly interested in $F_y$ as illustrated in Figure 5, we identify the same behavior for the load-displacement curve as observed in [9] and [15] (here the both referenced studies have been carried out for elasticity).

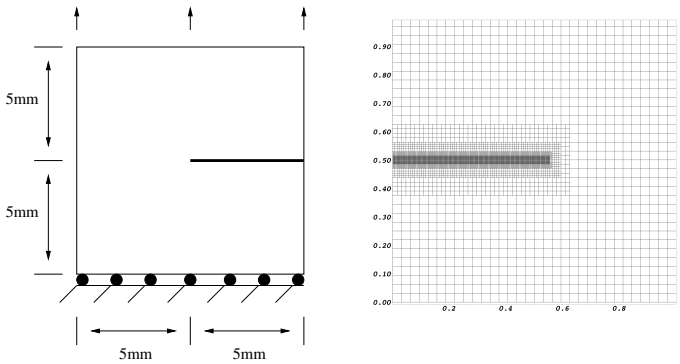


Figure 3: Example 4.1: Single edge notched tension test: configuration (left) and mesh. Here, on the bottom in $y$-direction, the specimen is fixed, and we have a Dirichlet boundary force in $y$-direction on the top boundary.

In Figure 4, we identify the crack pattern for three different displacement steps for the elastic test case. The locally pre-refined mesh is displayed in Figure 3.

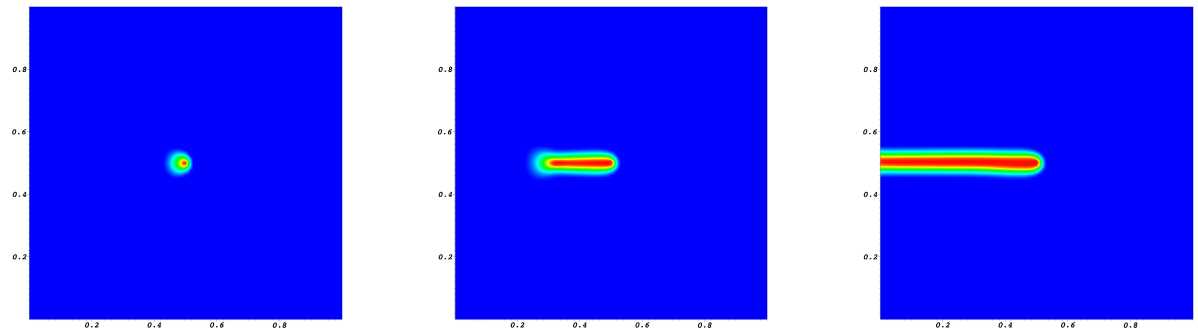

Figure 4: Example 4.1: Single edge notched tension test: crack pattern for three different displacement steps.

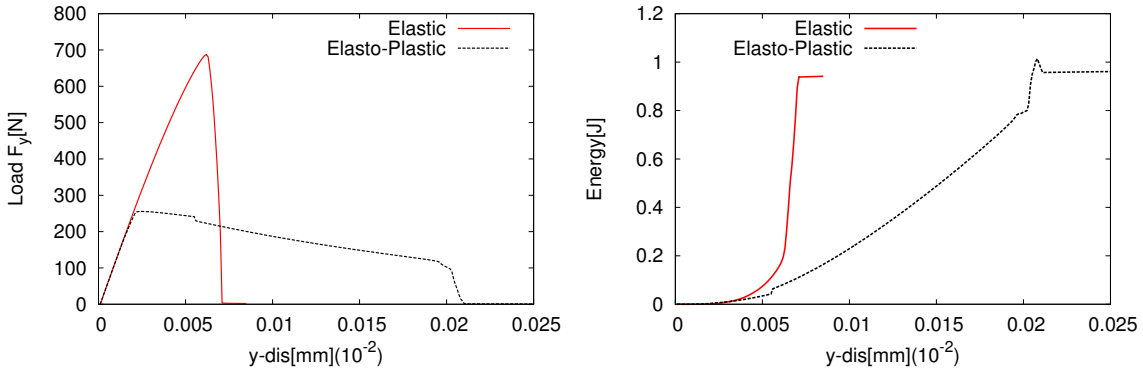


Figure 5: Example 1: Single edge notched tension test: load-displacement curves (left) and crack energies elasticity and elasto-plasticity. The load is measured along the top boundary. In both plots, we observe the influence of plasticity. In the left figure, the surface load on the top boundary is much lower in the elasto-plasticity setting because energy is dissipated to plastic regions. In contrast, the energy drop in elasticity is unstable and brutal. In the right figure, the crack energy increase (and therefore the crack development) is much slower in elasto-plasticity than in elasticity.

## 4.2 A screw tension test with elastic and elasto-plastic materials

In this section, the previous benchmark setting is extended to a realistic screw tension test. In addition to numerical findings, experimental results are used to compare crack pattern and material failure in screw production.

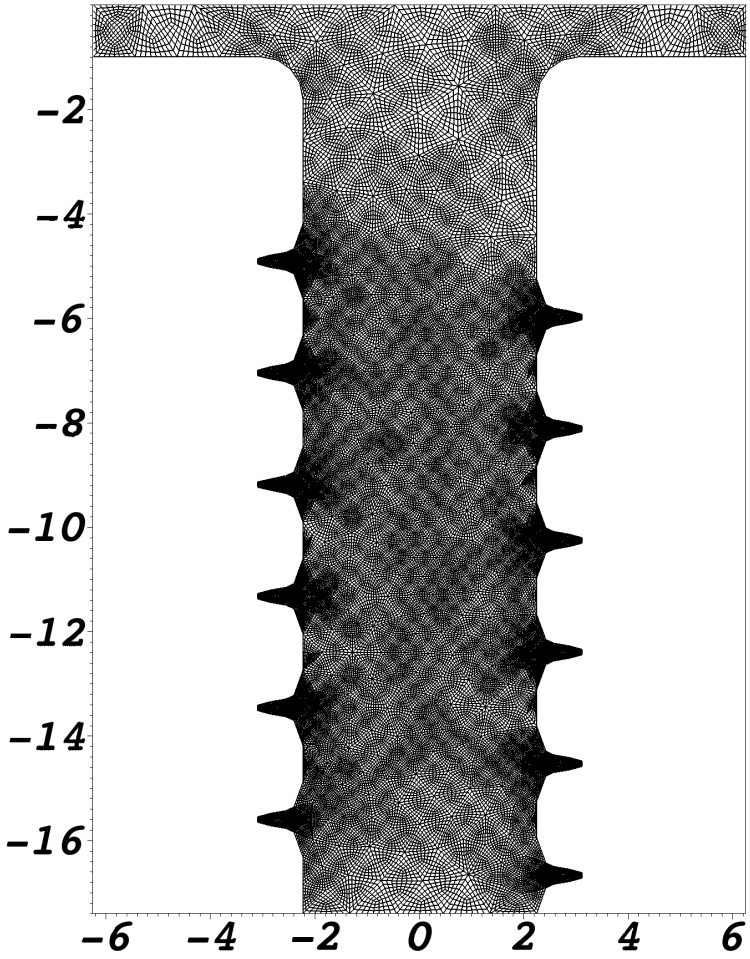


Figure 6: Examples 4.2: Mesh of screw simulation. The screw is fixed at the bottom, at top we have non-homogeneous Dirichlet conditions in $y$-direction (uniform tension). The units are in $mm$.

*Description and setup*

The production of screws usually takes place on a rolling machine. In this type of thread rolling the tools penetrate directly to the core diameter of the screw at the beginning of the forming process and displace the material of the workpiece to form a thread flank. This means that the thread flank comes into being step by step due to the material flow in the rolling dies. In this way a closing wrinkle is formed in the middle of thread flanks. If the set up of the rolling machine is not correctly or there is a

bad wire quality or incorrect dimensions of the bolt or already used rolling tools, material damage in the form of cracks or hollow-rolled screws is likely. Due to the increasingly safety-related applications, the demands on the rolled threads are immensely increasing, so cracks inside the screws can hardly be tolerated. Numerous experimental tests were carried out by provoked faulty set ups of the rolling machine in order to investigate the effects of cracks and hollow-rolled screws with different positions and lengths of the cracks. These screws were investigated with typical metallographic methods to characterize the material damage. The experimental tensile tests are qualitatively compared with finite element simulations. For the finite element simulation, the screw was meshed as a 2D model with the open source software gmsh [28], see Figure 6. The overall number of elements is specified below. As usually done in engineering and industrial applications, we focus on 2D simulations since here the computational cost is much less. These 2D simulation findings are then compared with 3D experimental tests in order to gain a first understanding of cracks and damage as well as mechanisms of failure in screws.

*Configuration, geometry, and mesh*

We consider a screw geometry which is designed according to experimental data. The screw geometry is displayed in Figure 6 and has a total length of $17.20mm$ and (outer) radius of $3mm$. We work on globally and locally refined meshes with hanging nodes. Specifically, in the main Section 4.2.1, the simulation is performed on three different mesh levels in order to check mesh sensitivity. Here, the levels $L = 1 + 0$ (once globally refined), $L = 1 + 1$ (once globally and once locally in the top region $-5mm \leq y \leq 0mm$), and $L = 1 + 2$ (once globally and two times local refinement) are considered. Level $1 + 0$ has 13760 mesh elements, $L = 1 + 1$ has 20360 mesh elements, and $L = 1 + 2$ has 46580 mesh elements.

*Boundary conditions*

The crack growth is driven by a non-homogeneous Dirichlet condition for the displacement field $u$ on $\Gamma_{top}$, the head of the screw at $y = 0.0$. We increase the displacement on $\Gamma_{top}$ at each time step such that the head is pulled, namely

$$u_y = \Delta t \times \bar{u}, \quad \bar{u} = 1.0 \text{ mm},$$

where $\Delta t = 10^{-2}$s. This is in agreement with experimental setups and corresponds to a constant pulling-velocity. On the bottom at $y = -16mm$, the screw is fixed, which corresponds to homogeneous Dirichlet conditions $u = 0$. On the remaining boundaries we prescribe stress-free conditions, i.e., homogeneous Neumann boundary conditions. For the phase-field variable $\varphi$ we prescribe as usually done stress-free conditions (homogeneous Neumann conditions) on all outer boundaries.

*Parameters*

We keep the material parameters as in the previous examples. As model parameters, we choose $\gamma = 100$, $\kappa = 10^{-6}h, \epsilon = 2h$ mm, and we perform the computations until the screw is damaged, which is dependent on the specific example and usually occurs between 20 and 40 increment time steps.

*Quantities of interest and mesh sensitivity*

As quantities of interest, the total time $T$ is taken into account when the screw is fully damaged; secondly, the time when the cracks start growing; and thirdly, the crack pattern. Finally, we also observe in the first test the numerical stability under mesh refinement. Here, we notice that the mesh

orientation is arbitrary and the crack is not aligned with mesh edges. Consequently, we can test if crack growth is independent of the underlying mesh (we also refer to [29], which discusses aspects when the crack follows the mesh or vice versa and additionally mesh sensitivity studies in [15] for a symmetric three point benchmark).

*Outline and motivation of the following numerical tests*

In the following, we provide different numerical simulations with increasing complexity. We first start with a completely undamaged screw without any cracks that is subject to tensile stresses. Next, a screw with cracks in thread flanks and cores is considered. In the final tests, a hollow-rolled screw is investigated. This final test is also the situation that is faced in the production processes of screws and it is important to understand the mechanisms under which circumstances cracks develop and then propagate.

### 4.2.1 Crack nucleation due to high stresses

In this first screw study, we investigate an intact screw that is subject to tensile loads and fixed at the bottom. This numerical set-up is ideal in the sense that we cannot run similar experimental tests since screws have always preexisting cracks. Consequently, a one-to-one comparison is not possible. Instead, we provide experimental results from fatigue tests with a few cycles that finally result in the same crack pattern as obtained from the numerical simulations. These numerical simulations with ideal screws offers fruitful insight that are not possible to gain with experiments. In the course of these tests, we notice that we take advantage of one of the major advantages of the phase-field approach for crack modeling, namely its capability for crack nucleation. These exactly develop in regions with highest stresses. However, as for example discussed in [30, 8] the length-scale parameter $\varepsilon$ can be interpreted as a material parameter and therefore has an influence on the nucleation process as remarked in [10]. Specifically, as shown in our discussion below, we agree with the findings presented in [10] (Section 2.3) that the nucleation stress goes to infinity as $\varepsilon \to 0$. In other words, the smaller $\varepsilon$, the later the crack will damage the screw head.

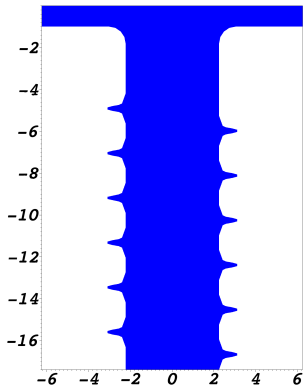


Figure 7: Example 4.2.1: Initial phase-field distribution with no cracks; i.e., $\varphi = 1$ in the entire domain.

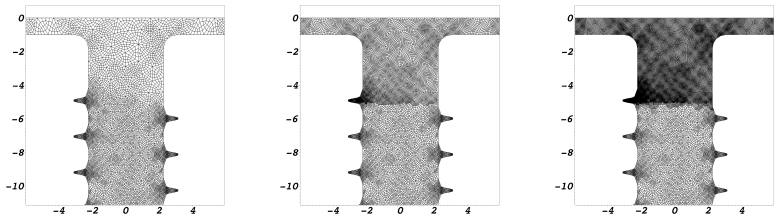

Figure 8: Example 4.2.1 in which cracks nucleate due to high stresses: Global mesh $L = 1 + 0$ and locally refined meshes $L = 1 + 1$ and $L = 1 + 2$. The units are in $mm$.

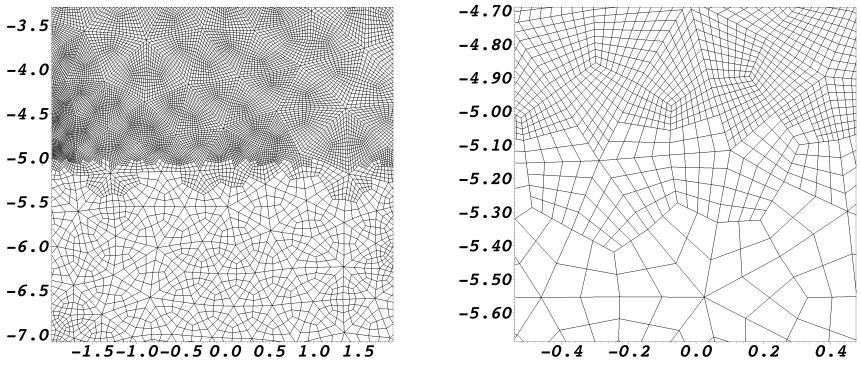

Figure 9: Example 4.2.1 in which cracks nucleate due to high stresses: Zoom-in to the locally refined mesh $L = 1 + 2$ to illustrate the hanging nodes in which the corse mesh matches the finer mesh. The units are in $mm$.

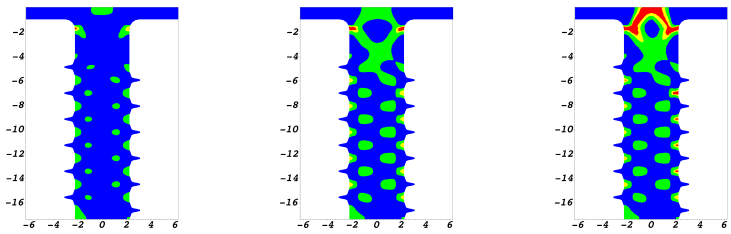

Figure 10: Example 4.2.1 on level $L = 1 + 0$ and $\varepsilon = 0.058mm$ in which cracks nucleate due to high stresses: Phase-field variable for different times $T = 14, 15, 16$ [s]. As before, cracked regions are denoted in red. We identify that the cracks develop at $T = 14s$ which corresponds to a displacement of $0.14mm$. The screw fails at $T = 16s$. We notice that due to the coarse mesh green islands develop with $\varphi \sim 0.7$, which however have no influence on the final crack path. This argument is justified because these islands vanish under mesh refinement (see Figure 11 and 12) but the final crack pattern remains the same. Consequently, our approach is numerically stable. The spatial units are in $mm$.

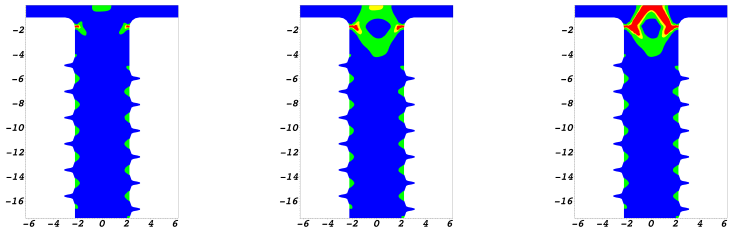

Figure 11: Example 4.2.1 on level $L = 1 + 1$ and $\varepsilon = 0.029mm$ in which cracks nucleate due to high stresses: Phase-field variable for different times $T = 18, 19, 20$ [s]. As before, cracked regions are denoted in red. We identify that the cracks develop at $T = 18s$ which corresponds to a displacement of $0.18mm$. The screw fails at $T = 20s$. The spatial units are in $mm$.

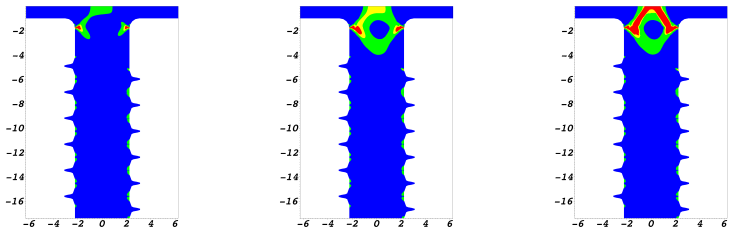

Figure 12: Example 4.2.1 on level $L = 1 + 2$ and $\varepsilon = 0.0145mm$ in which cracks nucleate due to high stresses: Phase-field variable for different times $T = 24, 25, 26$ [s]. As before, cracked regions are denoted in red. We identify that the cracks develop at $T = 24s$ which corresponds to a displacement of $0.24mm$. The screw fails at $T = 26s$. The spatial units are in $mm$.

First in Figure 7 the initial phase-field distribution is shown, i.e., $\varphi = 1$ in the entire domain. In Figure 8, we provide different spatially-refined meshes that are used for the finite element simulations. A zoom-in is provided in Figure 9 displaying the hanging-nodes where the fine mesh changes to a coarser mesh. Our first results in the Figures 10, 11, and 12, first demonstrate that the crack path is independent of the mesh by a sequence of snapshots at different times displaying the crack pattern. This is an essential observation because it is of most importance that the phase-field method does not depend on the mesh. Here, we also refer to [29] who introduce anisotropic mesh refinement and discuss several aspects of mesh-dependence. Further detailed studies if crack growth is independent of the mesh are provided in [12] and [15]. Secondly, our findings show that with regard to the choice of the length-scale parameter, we observe that the crack nucleates later for smaller $\varepsilon$. Finally as expected, we observe that the fracture develops in the head-piston region where the stresses are high. We notice that the crack propagates quickly within two time steps. This is expected behavior in brittle materials using elasticity as underlying solid model.

These results are now compared to elasto-plastic materials. Here as in the first example, the plastic flow rule is chosen as $\sigma_0 = \sqrt{2/3} \cdot 450$ [21] and fixed. The energy release rate $G_c$ is kept fixed. For other modeling choices of $G_c$, we refer the reader to [17] and [19]. In elasto-plastic settings we expect moderate crack propagation in comparison to brittle materials. Indeed observing the time steps of crack development in Figure 12 for brittle materials and in Figure 13 for ductile fracture in elasto-plasticity, the crack development in the elasto-plastic material is much more moderate than in brittle modeling.

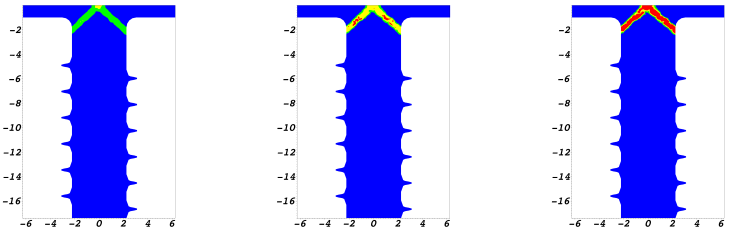

Figure 13: Example 4.2.1: Crack propagation (in red) in elasto-plasticity at times $T = 10, 20$ and $T = 30$ using $G_c = 2.7N/mm$ (as for the elastic case). Similar pattern are obtained for $G_c = 5.4N/mm$. However, in that case the final pattern is obtained at time step 45 for which we also refer to Figure 14. The spatial units are in $mm$.

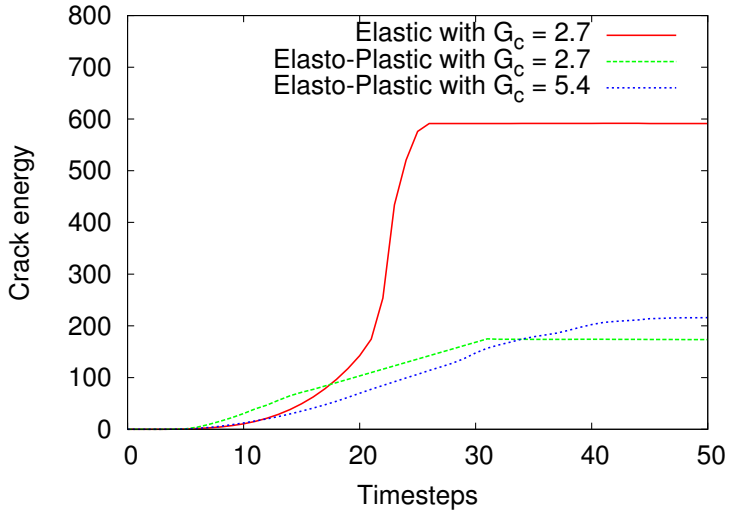


Figure 14: Example 4.2.1: Comparison of the crack energies for three different test cases with graphical results shown in Figures 12 and 13. The unit for the crack energy is $J$ and for the time steps $s$.

In Figure 14, crack growth is studied in pure elastic materials with $G_c = 2.7N/mm$, elasto-plastic with the same energy release rate $G_c = 2.7N/mm$ and finally elasto-plastic with a higher energy release rate $G_c = 5.4N/mm$. The crack energy increases once the crack starts developing and then propagating. Here, in the elasto-plastic setting with $G_c = 2.7N/mm$, the crack starts slightly earlier in its formation around time step 7 whereas the other two start at time step 9. After this we clearly see expected behavior, the crack in elasticity (brittle crack growth) becomes brutal and very fast between time steps $21-25$ until the material is broken and the energy remains therefore constant. In the broken material, no new cracks develop and consequently the crack energy does not further increase. In the elasto-plastic settings (ductile fracture), the crack formation and propagation is much slower and the final crack energy much less than in the elastic setting. In the case with $G_c = 2.7N/mm$, the material is broken at time step 30 and in the $G_c = 5.4N/mm$ test case, the material is completely damaged at time step 45. All results are reasonable and show well expected behavior since crack growth in brittle material is brutal whereas in elasto-plasticity the transition from undamaged to broken material is much longer and for the same setting, the elasto-plastic material is broken after its corresponding

elastic setting. We finally recall that the energy release rate should be higher in plasticity due to plastic dissipation. In our work, we just choose a higher number for the energy release rate and refer to the literature, e.g., [17, 19] and similar references for other modeling choices. In our work, we compare the elastic $G_c$ to a number that is twice higher.

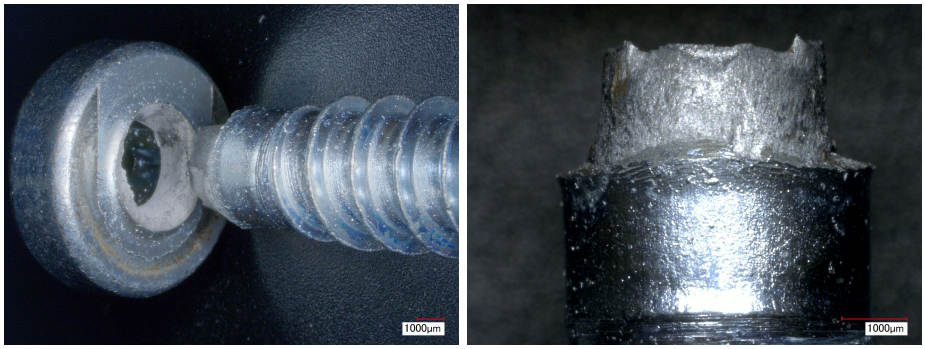


Figure 15: Example 4.2.1: Comparison to experimental tests in which the screw fails at the same point as obtained in the numerical simulation.

In Figure 15, experimental results are displayed. These results were obtained from a fatigue test with only a few cycles. It is interesting to notice that the crack behavior of the experimental fatigue test corresponds to the numerical results of the tensile test of the undamaged screw. Despite the fact that these configurations are not the same we can draw relevant conclusions from it. It is known that under high (notched) stresses the head of the screw will be cracked whereas low (cyclic) stresses lead to lower (notched) stresses near the head but induce cracks due to fatigue in the flanks and cores where initially closed wrinkle cracks were present. Under high loads, the local stresses in the head-piston region are responsible for the damage. Since in experimental setups, testing without any pre-existing cracks is not possible, we performed these numerical simulations and *compared* it to the most reasonable corresponding experimental set-up.

### 4.2.2 Two cracks in the thread flank and two cracks in cores (Part I) and cracks in all thread flanks and all cores (Part II)

We extend the previous example and prescribe initial cracks in the thread flanks and cores, which is motivated by experimental data as displayed in Figure 16. The goal of this test is to detect which cracks (i.e., in the flanks or cores) contribute to material failure. In the first set of computations, two cracks in flanks and cores are assumed. Then, we perform a second set of tests in which initial cracks in all flanks and cores are given. In contrast to the previous example, the screw is now initially damaged between the cores instead of the head. The goal in performing two sub-tests is to study if the number of initial cracks and their location contributes to damage.

Good agreement of the crack pattern between experimental results and numerical simulations is observed in the Figures 18 and 19. Furthermore, it is monitored that the crack growths at 45° degrees to the main principal stresses. The experimental results of a tensile test with screws is shown in Figure 16. After crack initiation in the core of the screw there is crack propagation in a 45° angle to the principal normal stress. This type of ductile failure as shown in Figure 16 was observed at all samples with cracks in the flanks and cores of the screw.

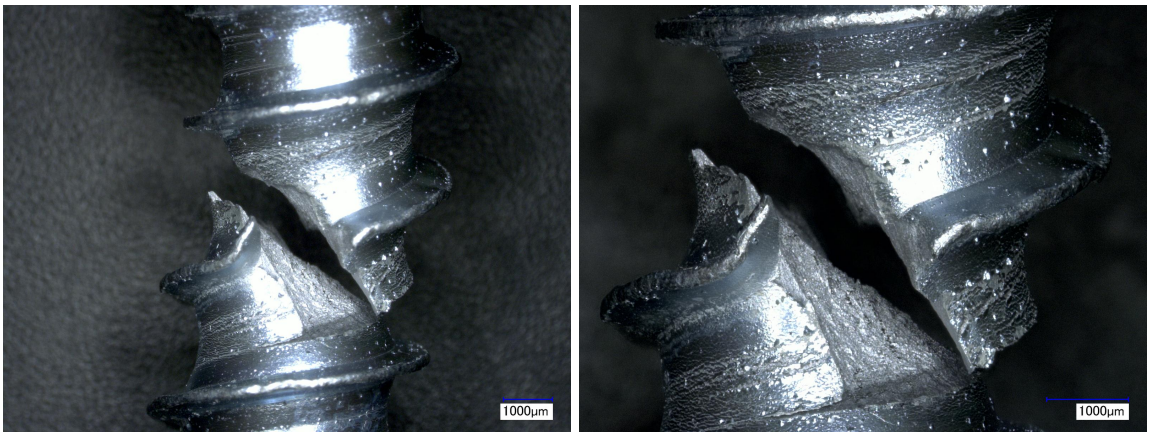


Figure 16: Examples 4.2.2: Experimental test. The crack propagates 45° degree to the main tensile principal stress. These pictures show a typical failure after a tensile test of screws.

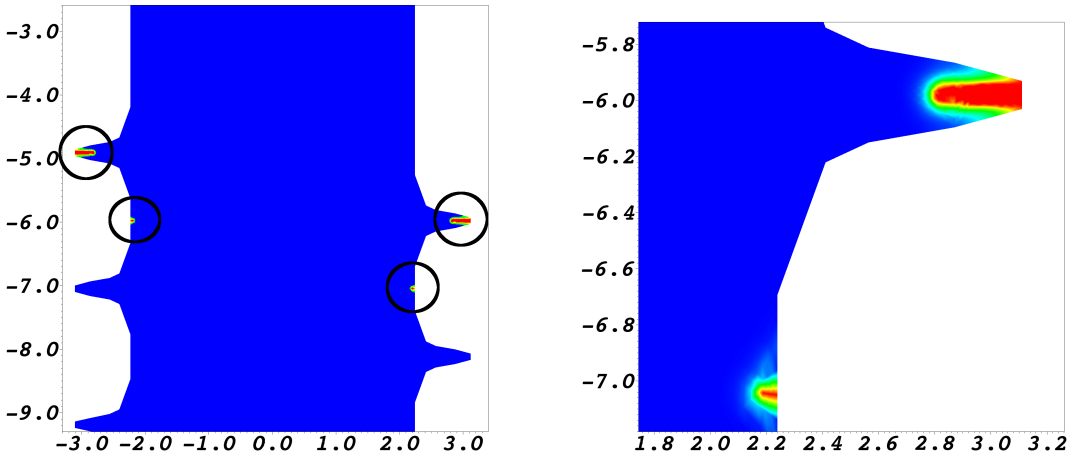


Figure 17: Example 4.2.2: Elastic brittle material in which four initial cracks are described in the flanks and cores. As before, cracked regions are denoted in red. The unit is in $mm$.

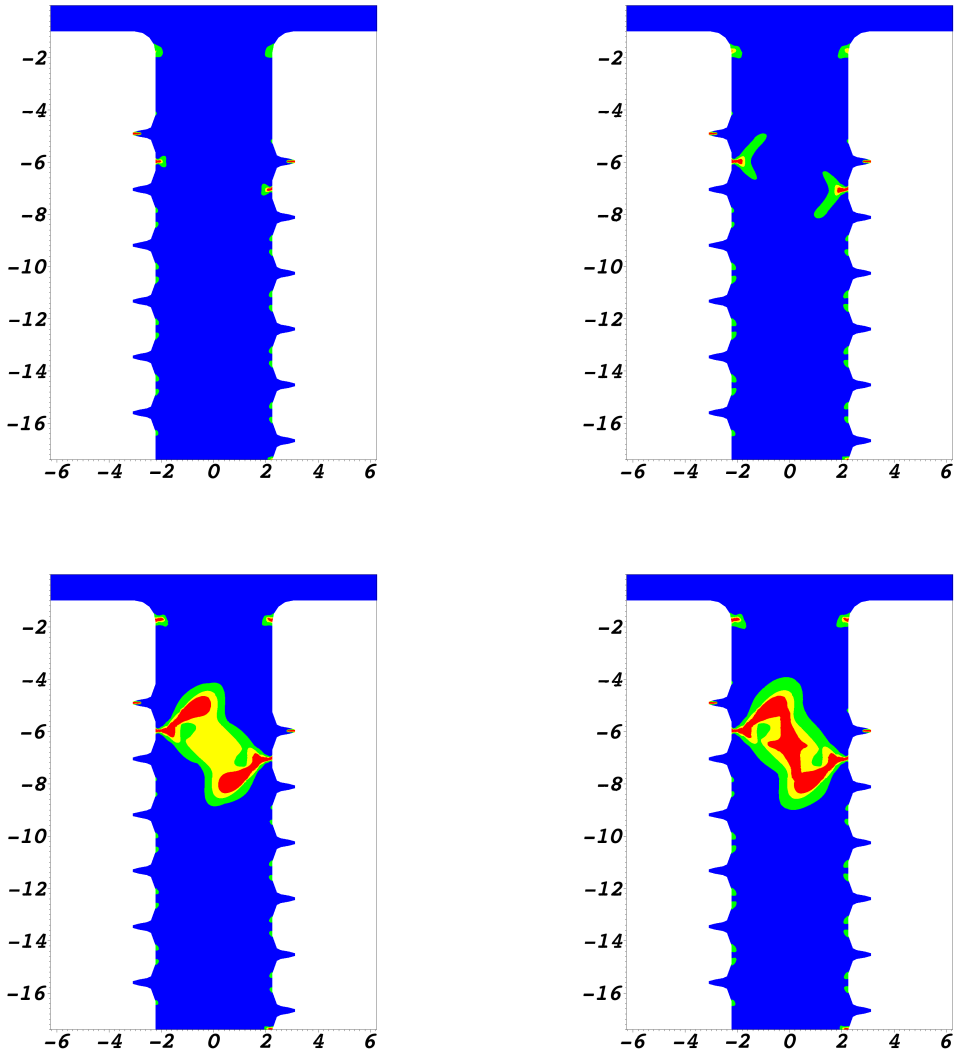


Figure 18: Example 4.2.2: Elastic brittle material in which two cracks are described in the flanks and cores. Here, the phase-field variable is shown at different times $T = 14s, 16s, 19s, 20s$. As before, cracked regions are denoted in red. The unit is in $mm$.

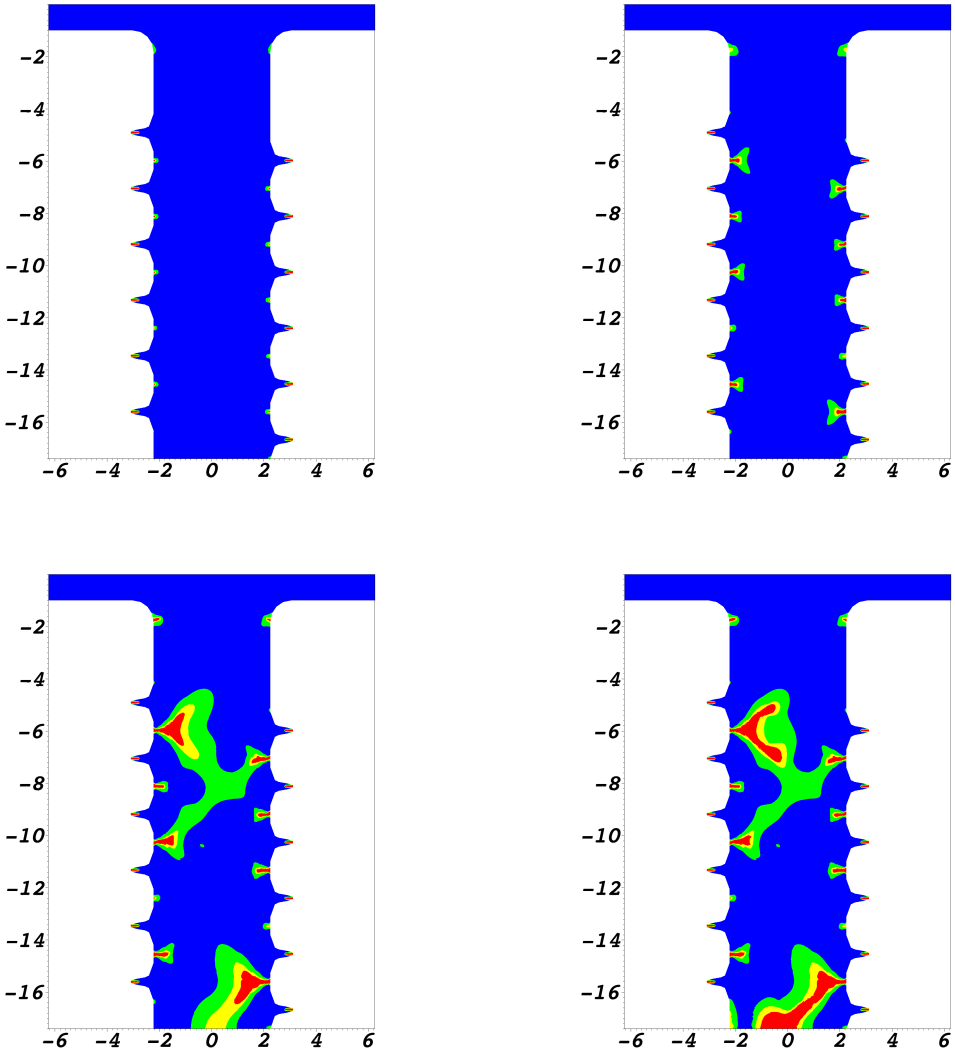


Figure 19: Example 4.2.2: Elastic brittle material in which initial cracks are described in all flanks and cores: Phase-field variable at different times $T = 14s, 16s, 19s, 20s$. As before, cracked regions are denoted in red. The unit is in $mm$.

### 4.2.3 Cracks in all flanks and cores and 3mm-in-length hollow-rolled screw

In addition to the previous tests, we now assume a hollow-rolled region inside the screw. This is a common artefact during the production process of screws as illustrated in Figure 1. In these two final elastic examples, we study the influence of the hollow-rolled region on crack propagation in tension. The experimental result of a crack is displayed in Figure 20. As also seen in the numerical simulations, the screw will crack between two core regions. In addition, the head of the screw is still intact (at left), which is in contrast to the crack nucleation tests from Section 4.2.1. Experimental data and numerical simulations show good agreement in the qualitative propagation of cracks.

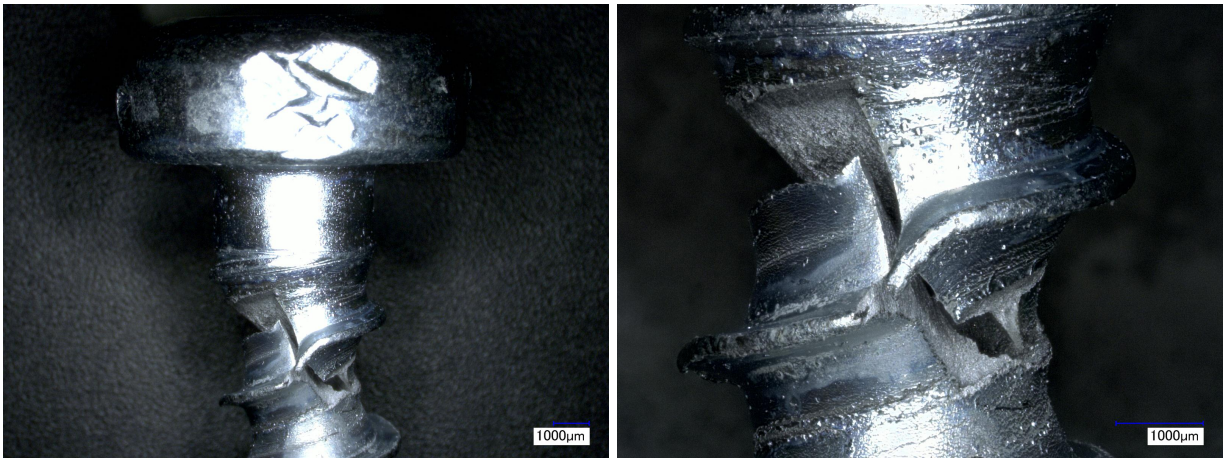


Figure 20: Examples 4.2.3 and 4.2.4: Experimental test with a hollow-rolled region.

This type of crack propagation is the same as described before, but the position of the ductile failure is slightly closer to the head of the screw. The crack pattern obtained from simulations are shown in Figure 21. Therein we observe that the material starts damaging (indicated in green color) in certain regions until these parts are fully cracked (indicated in red color).

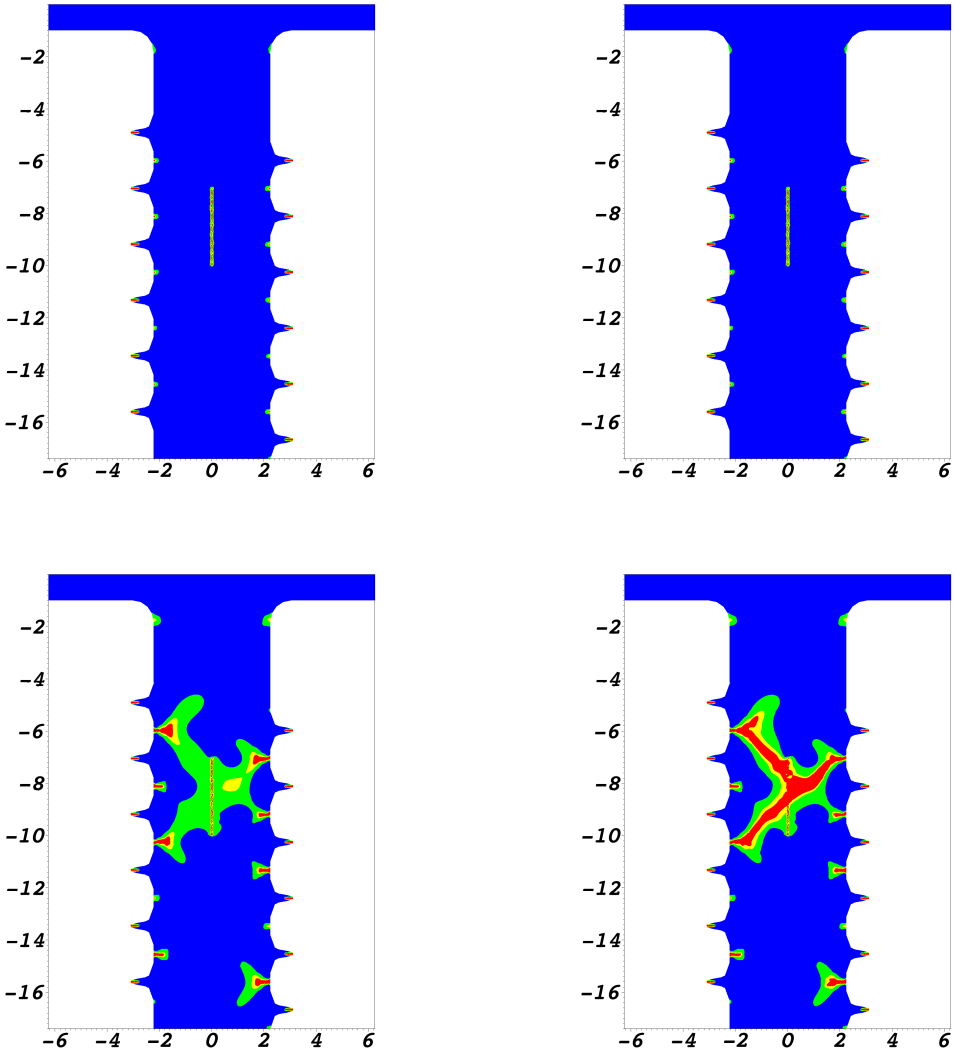


Figure 21: Example 4.2.3 in an elastic brittle material with initial cracks in all flanks and cores and the $3mm$ hollow-rolled screw: Phase-field variable. As before, cracked regions are denoted in red. Crack pattern (in red) at $T = 0s, 14s, 18s$ and $T = 19s$. In comparison to the previous two tests displayed in Figure 19 and 18, the screw is damaged $1s$ earlier, which is also reasonable from a material science point of view. In addition, we see crack branching, coalescing and non-planar growth. The unit is in $mm$.

### 4.2.4 Cracks in all flanks and cores and 6mm-in-length hollow-rolled screw

In this example, we extend the hollow-rolled region to $6mm$. In addition, we compare again between brittle material and elasto-plastic modeling.

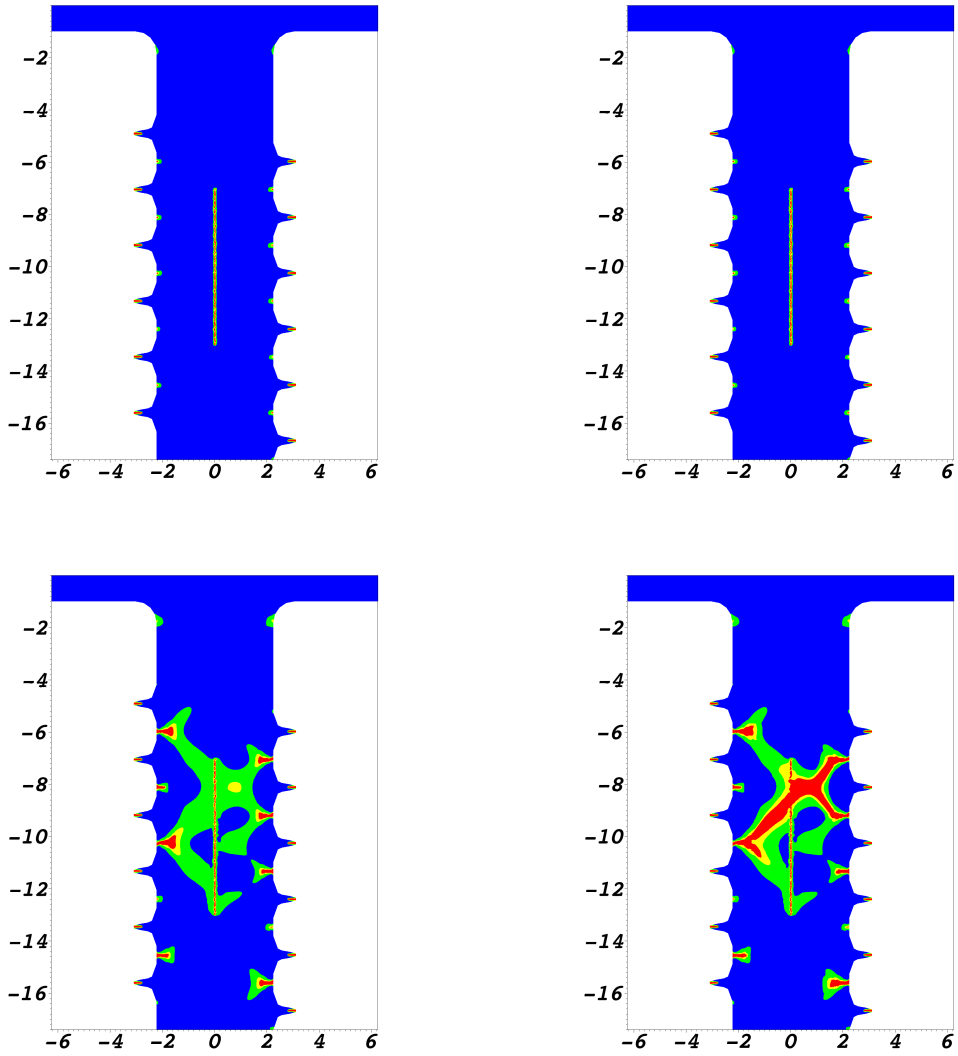


Figure 22: Example 4.2.4 in a brittle material with initial cracks in all flanks and cores and the $6mm$ hollow-rolled screw: Crack propagation (in red) at $T = 0s, 14s, 18s, 19s$. Similarly to the previous test, the screw is damaged at $T = 19s$. All spatial units are in $mm$.

First, we observe that crack initiation takes place in the thread core between the third and the fourth thread flank. Furthermore, our findings show different final crack pattern (see Figure 22 and 23); however both cracks grow again in a 45° angle which confirms the experimental observations. In addition, we see the same behavior as in Test 4.2.1; namely that ductile cracks develop earlier but the material needs longer to be completely cracked.

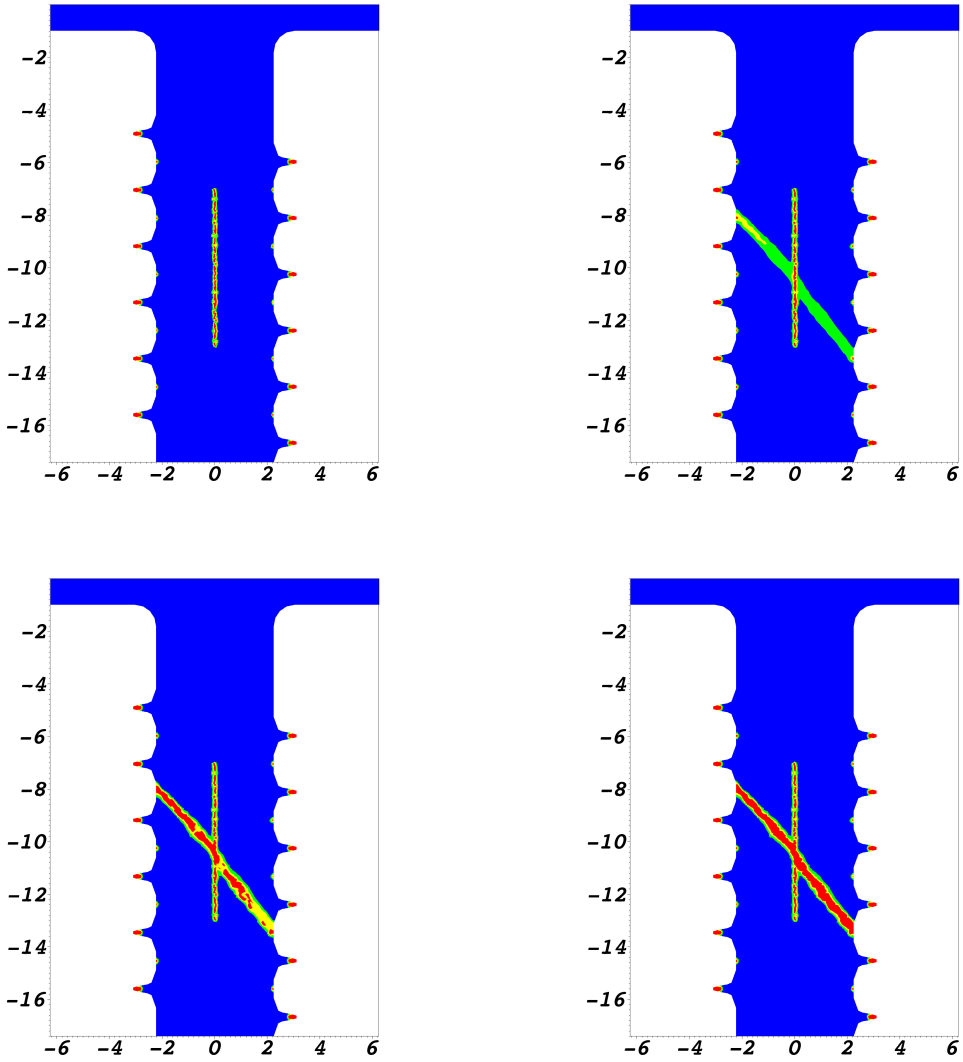


Figure 23: Example 4.2.4: Elasto-plastic material. Crack pattern (in red) at $T = 0s, 7s, 11s$ and $T = 15s$. The spatial units are in $mm$.

Here, crack propagation starts in the brittle material at $T = 17s$ and grows extremely fast. Two seconds later the sample fails. In contrast to Figure 22 it can be seen in Figure 23 that the crack starts to grow at T= 7s and the final failure is at point T= 15s. This can be interpreted as a stress relaxation based on plasticity, which is well-known, e.g., observing the strain-stress diagram. In contrast to our elastic settings, we observe that the crack path develops differently here. In particular at $11s$, the damage concentration varies over the crack. In fracture propagation this is rather uncommon whereas in damage science, such phenomena are known. In this respect we notice that phase-field fracture models have been recently linked to gradient damage models [30]. The final conclusion of our simulations presented in Figure 23 whether these phenomena are linked to a numerical instability or represent other effects is therefore left open for future research.

## 5 Conclusions

In this work, we proposed a phase-field formulation to solve crack propagation problems in elasticity and elasto-plasticity with final application to screw tension tests. Our approach consists of an elasto-plastic crack propagation formulation with a thermodynamically consistent phase-field model and its rate-dependent formulation within a robust augmented Lagrangian solution algorithm. First, benchmarks for code verification were considered. Then, the program code was used to simulate crack propagation in screws. Here, several different configurations were considered that included no initial material failure, initial cracks in flanks and thread cores, and initial cracks due to hollow-rolled regions. The simulation findings show that the presence of cracks in the thread flanks is less dangerous than initial cracks in the thread cores and a hollow-rolled region in the middle of the screws. Furthermore, it can be seen that the final failure of the hollow-rolled screw employing elasto-plastic material behavior starts earlier compared to the same setting without hollow-rolled area. Experimental verification tests show the same crack pattern and failure as obtained by numerical simulations. In conclusion, the numerical tests provided more insight on the effects of different positions and lengths of cracks in screws than only carrying out experiments. Moreover, experiments are not easy to carry out in general, specifically for the hollow-rolled screws such that numerical simulations are indispensable to better understand their material failure.

## Acknowledgments

The second author thanks F.-T. Suttmeier (University of Siegen) for a brief discussion on formulations for rate-dependent elasticity and plasticity during the preparation of this paper.

## References

[1] A. Griffith, The phenomena of rupture and flow in solids., Philos. Trans. R. Soc. Lond. 221 (1921) 163–198.

[2] N. Moes, J. Dolbow, T. Belytschko, A finite element method for crack growth without remeshing, Int. J. Numer. Methods Engrg. 46 (1999) 131–150.

[3] I. Babuska, U. Banerjee, Stable generalized finite element method (sgfem), Comput. Methods Appl. Mech. Engrg. 201-204 (2012) 91–111.

[4] I. Babuska, J. Belenk, The partition of unity method, Int. J. Numer. Methods Engrg. 40 (1997) 727–758.

[5] G. Francfort, J.-J. Marigo, Revisiting brittle fracture as an energy minimization problem, J. Mech. Phys. Solids 46 (1998) 1319–1342.

[6] B. Bourdin, G. Francfort, J.-J. Marigo, Numerical experiments in revisited brittle fracture, J. Mech. Phys. Solids 48 (2000) 797–826.

[7] B. Bourdin, G. Francfort, J.-J. Marigo, The variational approach to fracture, J. Elasticity 91 (2008) 1–148.

[8] C. Miehe, F. Welschinger, M. Hofacker, Thermodynamically consistent phase-field models of fracture: variational principles and multi-field fe implementations, International Journal of Numerical Methods in Engineering 83 (2013) 1273–1311.

[9] C. Miehe, M. Hofacker, F. Welschinger, A phase field model for rate-independent crack propagation: Robust algorithmic implementation based on operator splits, Comput. Meth. Appl. Mech. Engrg. 199 (2010) 2765–2778.

[10] M. J. Borden, C. V. Verhoosel, M. A. Scott, T. J. R. Hughes, C. M. Landis, A phase-field description of dynamic brittle fracture, Comput. Meth. Appl. Mech. Engrg. 217 (2012) 77–95.

[11] M. Hofacker, C. Miehe, Continuum phase field modeling of dynamic fracture: variational principles and staggered FE implementation, Int. J. Fract. 178 (2012) 113–129.

[12] M. Wheeler, T. Wick, W. Wollner, An augmented-Lagangrian method for the phase-field approach for pressurized fractures, Comp. Meth. Appl. Mech. Engrg. 271 (2014) 69–85.

[13] M. Tonks, D. Gaston, P. Millett, D. Andrs, P. Talbot, An object-oriented finite element framework for multiphysics phase field simulations, Computational Materials Science 51 (2012) 20–29.

[14] S. Burke, C. Ortner, E. Süli, An adaptive finite element approximation of a variational model of brittle fracture, SIAM J. Numer. Anal. 48 (2010) 980–1012.

[15] T. Heister, M. F. Wheeler, T. Wick, A primal-dual active set method and predictor-corrector mesh adaptivity for computing fracture propagation using a phase-field approach, Computer Methods in Applied Mechanics and Engineering 290 (2015) 466 – 495.

[16] M. Hofacker, C. Miehe, A phase-field model for ductile to brittle failure mode transition, Proc. Appl. Math. Mech. 12 (2012) 173–174.

[17] H. Ulmer, M. Hofacker, C. Miehe, Phase field modeling of brittle and ductile fracture, PAMM 13 (2013) 533–536.

[18] F. Duda, A. Ciarbonetti, P. Sanchez, A. Huespe, A phase-field/gradient damage model for brittle fracture in elastic-plastic regimes, Int. J. Plast. 65 (2015) 269–296.

[19] M. Ambati, T. Gerasimov, L. de Lorenzis, Phase-field modeling of ductile fracture, Comput. Mech. (2015).

[20] G. Duvaut, J. L. Lions, Inequalities in mechanics and physics, Grundlehren der mathematischen Wissenschaften, Springer, Heidelberg, 1976.

[21] E. Stein, Error-controlled adaptive finite elements in solid mechanics, John Wiley, 2002.

[22] R. Rannacher, F. Suttmeier, Error estimation and adaptive mesh design for FE models in elastoplasticity (2000), John Wiley, E. Stein, ed. edition.

[23] C. Goll, T. Wick, W. Wollner, DOpElib: Differential Equations and Optimization Environment Library, 2010.

[24] W. Bangerth, T. Heister, G. Kanschat, et al., Differential Equations Analysis Library, 2012.

[25] L. Ambrosio, V. Tortorelli, Approximation of functionals depending on jumps by elliptic functionals via $\gamma$-convergence, Comm. Pure Appl. Math. 43 (1990) 999–1036.

[26] L. Ambrosio, V. Tortorelli, On the approximation of free discontinuity problems, Boll. Un. Mat. Ital. B 6 (1992) 105–123.

[27] T. Wick, Solving monolithic fluid-structure interaction problems in arbitrary Lagrangian Eulerian coordinates with the deal.ii library, Archive of Numerical Software 1 (2013) 1–19.

[28] C. Geuzaine, J.-F. Remacle, Gmsh: a three-dimensional finite element mesh generator with built-in pre- and post-processing facilities, Int. J. Numer. Methods Engrg. 79 (2009) 1309–1331.

[29] M. Artina, M. Fornasier, S. Micheletti, S. Perotto, Anisotropic mesh adaptation for crack detection in brittle materials, 2014. TUM Report.

[30] K. Pham, H. Amor, J.-J. Marigo, C. Maurini, Gradient Damage Models and Their Use to Approximate Brittle Fracture, Int. J. of Damage Mech. (2011) 1–36.